Super-resolved total internal reflection fluorescence microscopy using random illuminations

Kévin Affannoukoué, Simon Labouesse, Guillaume Maire, Laurent Gallais, Julien Savatier, Marc Allain, Md Rasedujjaman, Loïc Le Goff, Jérôme Idier, Renaud Poincloux, et al.

Research Article Vol. 10, No. 8 / August 2023 / Optica 1009

Super-resolved total internal reflection fluorescence microscopy using random illuminations

Kévin Affannoukoué,[1] Simon Labouesse,[2] Guillaume Maire,[1] Laurent Gallais,[1] Julien Savatier,[1] Marc Allain,[1] Md Rasedujjaman,[1] Loic Legoff,[1] Jérôme Idier,[3] Renaud Poincloux,[4] Florence Pelletier,[5] Christophe Leterrier,[5] Thomas Mangeat,[2] and Anne Sentenac[1,*]

[1]Institut Fresnel, Aix Marseille Université, CNRS, Centrale Marseille, 13013 Marseille, France
[2]LITC Core Facility, Centre de Biologie Integrative, Université de Toulouse, CNRS, UPS, Toulouse 31062, France
[3]LS2N, CNRS UMR 6004, F44321 Nantes Cedex 3, France
[4]Institut de Pharmacologie et de Biologie Structurale, Université de Toulouse, CNRS, UPS, Toulouse 31062, France
[5]Aix Marseille Université, CNRS, INP UMR7051, NeuroCyto, 13005 Marseille, France
*anne.sentenac@fresnel.fr

Received 6 February 2023; revised 3 June 2023; accepted 11 June 2023; published 27 July 2023

A benefit of random illumination microscopy (RIM) is that it improves the resolution and linearity of the brightness of structured illumination microscopy using minimally controlled speckled illumination. Here, we implemented RIM in the total internal reflection fluorescence (TIRF) configuration for imaging biological processes close to the coverslip surface. Using standard TIRF objectives, we separated fluorescent lines 60 nm apart and achieved high contrast 86 nm resolution on fixed biological samples. Applied to live macrophages, TIRF-RIM provided two-color dynamic images of paxillin nanoclusters with remarkable spatial (96–120 nm) and temporal (1–8 Hz) resolutions, respectively. The simple experimental setup and imaging protocol together with the robustness of the data processing to leaks and aberrations make TIRF-RIM a method of choice for super-resolution TIRF imaging.

https://doi.org/10.1364/OPTICA.487003

1. INTRODUCTION

In multicellular organisms, the cells interact physically with their environment and with each other. They can deform their membrane, engulf objects such as viruses, and move. Cell membranes are the site of complex, dynamic processes involved in various physiological functions. Total internal reflection fluorescence microscopy (TIRFM) is best adapted for observing the cell membrane in action [1]. It exploits an evanescent field induced at the boundary between high and low refractive index media to selectively excite a very thin slice of the sample (from 100 to 300 nm, depending on the illumination angle) above the coverslip surface. The minimal exposure of the sample to light above the excitation slice markedly reduces both the out-of-focus fluorescence and the phototoxicity, which are two major issues in live-cell imaging.

However, the lateral resolution of total internal reflection fluorescence (TIRF) is diffraction limited to about 200–300 nm. In addition, the optical sectioning of the evanescent illumination of TIRF is rarely perfect. Propagative waves stemming from imperfections in microscope optics and/or from unavoidable light scattering by the sample itself excite the fluorescent markers present in the volume of the sample. These illumination leaks result in out-of-focus fluorescence detrimental to the image contrast [2–4].

In the past 20 years, most super-resolution methods have been adapted to the TIRF configuration, from stimulated emission depletion [5] to single molecule localization methods [6] and the recent Minflux [7]. Among them, structured illumination microscopy (SIM) presented a favorable trade-off between spatio-temporal resolutions and phototoxicity, making it well-suited for a wide range of applications in live-cell imaging [8,9]. In interference-based TIRF-SIM, the super-resolved image is formed numerically from several low-resolution images recorded under different positions and orientations of a light grid obtained from the interference of two opposite grazing collimated beams [10,11]. Interference-based TIRF-SIM yielded impressive dynamic images of the cytoskeleton [12] at a resolution (sub-100 nm, 2 Hz) twice as good as standard TIRFM, which could be further increased (sub-90 nm, 49 Hz) using sparsity and continuity regularizations in the reconstruction schemes [13,14]. Another TIRF-SIM technique based on the scanning of a matrix of evanescent spots and an analogical reconstruction offered a higher temporal resolution (from 0.8 to 100 Hz) at the price of a lesser lateral resolution (from 134 to 180 nm, respectively) [15]. These results were

obtained with ultra-high-numerical-aperture lenses (NA = 1.7). The major weakness of SIM lays in the accuracy with which the illumination pattern has to be known for the reconstruction to succeed. Slight errors on the light grid estimation yield artifacts in the reconstructed super-resolved image [16,17], which may lead to misinterpretation of biological structures, [18]. This issue is particularly apparent in TIRF-SIM where the small overlap between the shifted sample spectra renders the estimation of the grid parameters more demanding [17]. Hence, the effectiveness of TIRF-SIM reconstruction is compromised by factors such as large Stokes shifts, low signal-to-noise ratio, or low image contrast (caused by residual out-of-focus fluorescence or suboptimal polarization control of the illumination) [18]. In this context, the recently proposed random illumination microscopy (RIM) method [19] appeared to be an ideal technique for improving the performance of TIRF without the limitations and complexity of SIM. In RIM, the super-resolved image of the sample is obtained from the variance of low-resolution images recorded under random speckled illuminations. The advantages of RIM are multiple: with knowledge of the illuminations being unnecessary, large Stokes shifts, misalignment, and sample-induced distortions are not an issue; the reconstruction procedure avoids *a priori* information on the samples (binarity or sparsity constraints) and its inherent artifacts; and, the control of the illuminations being minimal, the RIM tuning and experimental protocol are similar to those of classical widefield microscopes [19].

In the present work, we have adapted RIM to the TIRF configuration. We explored the performance of TIRF-RIM on synthetic data, calibrated samples, and fixed cells. We found that TIRF-RIM provided images with a much better contrast and more than two-fold resolution gain compared to TIRF and were less affected by reconstruction artifacts than TIRF-SIM. Then, TIRF-RIM was used for imaging podosomes at the basal membrane of live macrophage cells. Using standard TIRF objectives with NA = 1.49, TIRF-RIM revealed the dynamics of paxillin nanoclusters with high spatio-temporal resolutions (120 nm, 0.12 s) and (96 nm, 1 s). Large Stokes shifts, low signal-to-noise ratio, and lack of contrast, due to residual out-of-focus, misalignement, or nonoptimal polarization control, make the estimation of the grid pattern problematic [17,18]. In this context, the recently proposed RIM method [19], appeared to be an ideal technique for improving the performance of TIRF without the limitations and complexity of SIM. In RIM, the super-resolved image of the sample is obtained from the variance of low-resolution images recorded under random speckled illuminations.

2. ADAPTATION OF RIM TO TOTAL INTERNAL REFLECTION CONFIGURATION

RIM is a widefield super-resolved imaging method that combines the SIM demodulation principle with fluctuation microscopy (SOFI) statistical processing [6,19–22]. A RIM super-resolved image is obtained by, first, forming the empirical variance of a few hundred images of the sample recorded under random speckled illuminations and, second, processing this variance using an inversion scheme (named AlgoRIM) that accounts for the spatial characteristics of the illumination [Fig. 1(a)]. Contrary to SIM, which requires knowledge of the illumination patterns, algoRIM needs only the illumination second-order statistics, namely the speckle autocorrelation function, for downmodulating the sample high frequencies. Likewise, contrary to SOFI and several high density localization methods that are based on the image variance, algoRIM does not rely on *a priori* information on the sample (such as binarity or sparsity), and its reconstructions are linear to brightness [19].

TIRF-RIM was implemented in a standard TIRF microscope using coherent illumination and an objective of numerical aperture NA = 1.49. The evanescent speckled light was obtained thanks to a diffuser [here a spatial light modulator (SLM)] placed at the (conjugated) image plane of the objective and an annular aperture positioned at the objective Fourier plane, which removed all the waves propagating below the glass–water critical angle [Fig. 1(b)]. We observed in Fig. 1(b) that the TIRF speckles at the focal plane differed markedly from the propagative speckles obtained by removing the annular aperture. The TIRF-speckled light grains were smaller and packed like strings of pearls, instead of being dispersed in the field of view. Indeed, a TIRF-speckle pattern can be modeled as the interference of Bessel beams placed at random. Now, Bessel beams exhibit important oscillations about their maximum and can be narrower than standard focused beams. The interference of these radially quasi-periodical features causes the stringy appearance of the TIRF speckles. The difference between standard speckles and TIRF speckles is reflected in the speckle autocorrelation displayed in Supplement 1 Fig. 5. The standard speckle autocorrelation spectrum decays rapidly with increasing spatial frequencies, while the TIRF one exhibits a plateau and peaks at high frequencies [12]. The data processing of TIRF-RIM was the same as for RIM [19] and is fully described in Section 6. In all the experiments, the observation point spread function and the speckle autocorrelation were estimated theoretically.

3. TIRF-RIM VERSUS TIRFM AND TIRF-SIM

In this section, we investigate the TIRF-RIM performance on fixed samples and synthetic data.

In Fig. 2(a), we compared TIRF-RIM and TIRFM on fixed COS cells fluorescently labeled for clathrin and tubulin (using Alexa Fluor 488 and Alexa Fluor 555 conjugated antibodies, respectively). The TIRF two-color image showed a residual fluorescence blur, likely due to illumination leaks, which dimmed the image contrast. TIRF-RIM reconstruction was better contrasted and resolved than the TIRF image thanks to the additional optical sectioning and resolution gain of RIM data processing. In particular, the ring shape of the clathrin-coated pits was clearly observed [12].

To evaluate quantitatively TIRF-RIM resolution, we imaged a calibrated Argo-SIM ruler (from Argolight) that displays fluorescent lines whose spacing gradually increases from 0 nm to 390 nm, in steps of 30 nm. Note that for the lines being placed 100 μm deep inside a glass slide, the TIRF conditions are not met. This experiment was mainly intended to study the performance of the reconstructions using TIRF-like speckles (i.e., speckles that have been formed through an annular pupil) instead of regular propagative speckles (without the annular aperture) as in standard RIM [19]. We found that, with 400 speckled images, TIRF-RIM distinguished the lines separated by 90 nm and almost disclosed the presence of lines separated by 60 nm. On the other hand, TIRFM could barely distinguish the lines separated by 180 nm; see Figs. 2(c)–2(e). Interestingly, TIRF-RIM had a better resolution than standard RIM, which did not distinguish the lines 60 nm apart [19]. The better resolution of TIRF-RIM as compared to

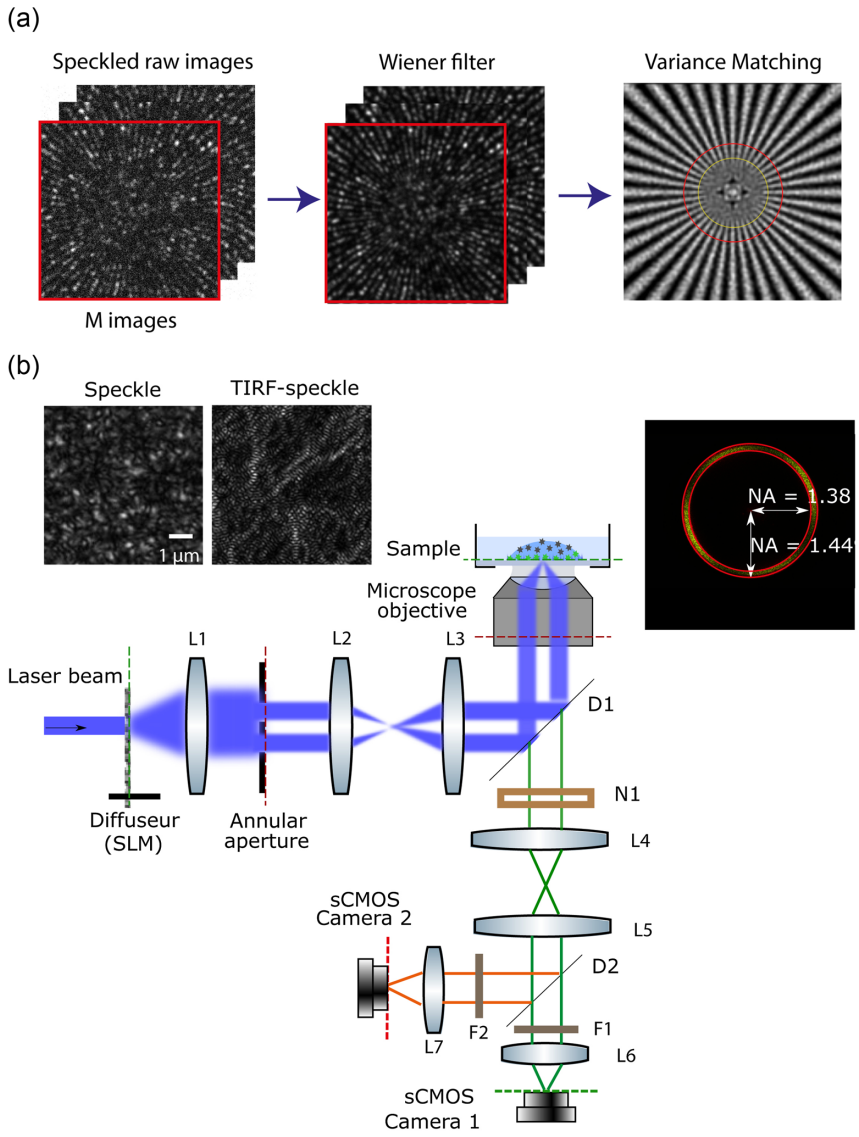

Fig. 1. TIRF-RIM principle. (a) Multiple images of the sample are recorded under different random speckled illuminations. Each raw speckled image is prefiltered using a Wiener filter to reduce the noise. The super-resolved reconstruction is obtained from the variance of the prefiltered images using AlgoRIM (Methods). The red circle indicates the resolution limit of standard fluorescence microscopy; the yellow circle illustrates the resolution gain brought by RIM. The star-like sample used in this illustration is visible in Supplement 1 Fig. 6 and defined in [19]. (b) Experimental setup. A standard TIRF microscope is modified by introducing a spatial light modulator (SLM) acting as a diffuser along the illumination path [the image (pupil) planes are indicated with green (red) dashed lines]. The diffuser is illuminated by a collimated laser beam to generate a speckle at the sample plane. An annular aperture, placed at the Fourier plane of the objective, blocks the incident waves that are not totally reflected at the glass–water interface of the sample support. In our experiment, two cameras are used to provide bicolor images (see Supplement 1 for more details on the setup). The top-right inset shows an experimental image of the incident intensity at the pupil plane in the presence of the annular aperture and indicates the lowest and highest numerical apertures defined by the inner and outer radii of the annulus. The top-left inset shows experimental images of one TIRF speckle and one standard speckle (without the annular aperture). The images of the incident light were obtained by placing a mirror at the focal plane and removing the dichroic mirror along the observation path.

standard RIM can be explained by the spectra of the speckle autocorrelation functions in Supplement 1 Fig. 5. The ratio between the high and null spatial frequencies of TIRF speckles being higher than that of standard speckles, one can expect the sample high spatial frequencies to be better transmitted to the image variance in the TIRF configuration.

Next, we compared TIRF-RIM to TIRF-SIM on synthetic data provided by a microscope simulator [23]. We considered a three-dimensional (3D) sample made of a fluorescent star-like pattern at the focal plane covered by a suspension of fluorescent beads mimicking sample volume as a potential source of out-of-focus blur, as shown in Supplement 1 Fig. 6. To take into account possible light leaks in our simulations, [1], we added to the evanescent RIM and SIM incident fields a propagative speckle field with intensity increasing from 1 to 10% of the total intensity measured at $z = 0$.

TIRF-SIM and TIRF-RIM reconstructions were obtained using codes freely available on the net, AlgoRIM and FairSIM.

In an ideal configuration (no leaks), the TIRF-SIM resolution gain was slightly better than that of TIRF-RIM and was less sensitive to a decrease in photon budget (Supplement 1 Fig. 7). This could be expected since, at similar global photon budget, the

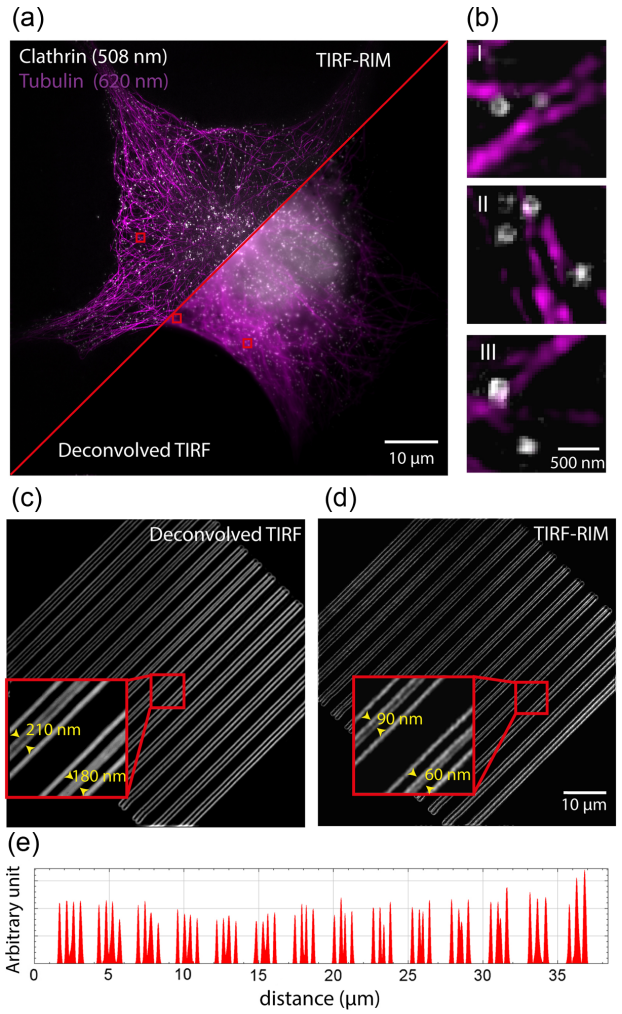

Fig. 2. TIRF-RIM (using 400 speckled images) versus TIRF microscopy. (a), (b) Images of a fixed COS cell labeled for clathrin (using an Alexa Fluor 488-conjugated secondary antibody) and tubulin (using an Alexa Fluor 555-conjugated secondary antibody). The illumination wavelength is 488 nm. (a) Deconvolved TIRF (bottom-right) and TIRF-RIM (top-left) images. In the TIRF image, the image contrast is dimmed by some out-of-focus fluorescence stemming from residual light leaks. TIRF-RIM improves both the image contrast and the resolution. (b) Zooms on the clathrin-coated pits as seen by TIRF-RIM. (c)–(e) Images of a calibrated Argo-SIM ruler. From bottom right to top left, the interdistance between the center lines increases from 0 to 390 nm in steps of 30 nm. The TIRF conditions are not met as the fluorescent lines are embedded in a glass slide, but, at variance with regular RIM, the speckles are formed through the annular aperture. (c) Deconvolved TIRF image: the lines separated by 180 nm are barely distinguishable. (d) TIRF-RIM using 400 speckled images. TIRF-RIM distinguishes the lines separated by 90 nm and discloses the presence of the lines 60 nm apart (see the inset). (e) TIRF-RIM signal integrated along the lines of the Argo-SIM ruler. The spacing of the center lines increases from 0 to 390 nm from right to left.

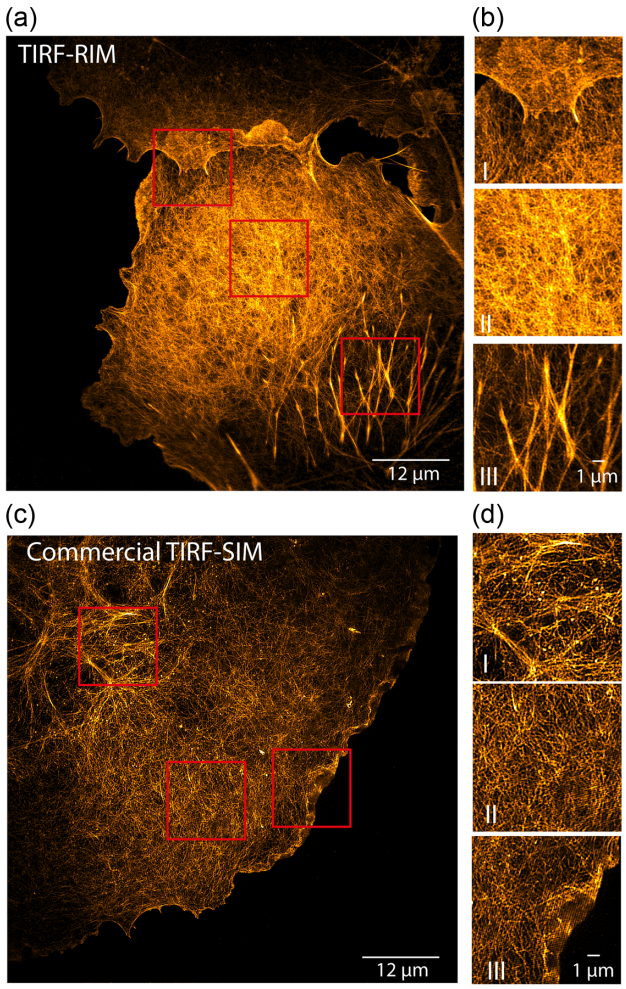

Fig. 3. Comparison of TIRF-RIM and TIRF-SIM on images of fixed COS-7 cells labeled for actin. Nine images are used for TIRF-SIM and 400 images in TIRF-RIM. A dozen cells were observed, and we present two representative images of this study. (a) TIRF-RIM reconstruction over a wide field of view. (b) Three zooms of (a) showing TIRF-RIM efficiency on both the sparse and dense regions and the absence of artifacts. (c) TIRF-SIM reconstruction (N-SIM commercial software) acquired on a sister coverslip sample. (d) Three zooms of (c) showing the presence of grid artifacts at different locations of the field of view. Note that among the dozen TIRF-SIM images, three presented no visible artifacts; see Supplement 1 Fig. 9.

400 RIM speckled images are significantly noisier than the nine SIM raw images and more likely to lose information on the high frequencies of the sample.

On the other hand, the quality of TIRF-RIM images was better maintained than that of TIRF-SIM in less than ideal configurations. Hence, when light leaks were present (due to a slight misalignement or induced by the sample itself) or when the Stokes shift was increased, we observed that TIRF-SIM reconstructions were affected by significant artifacts, whereas TIRF-RIM images were minimally perturbed (Supplement 1 Figs. 6 and 8A). The indifference of TIRF-RIM to large Stokes shifts was confirmed experimentally by comparing images of clathrin-coated pits (labeled with Alexa Fluor 488 and illuminated at 488 nm) obtained by filtering the emitted light at 508 nm (Fig. 2) and 630 nm (Supplement 1 Fig. 4B). Apart from an (expected) slight decrease of resolution in the large Stokes shift case, the images looked similar.

The robustness of TIRF-RIM in practical situations was further evidenced by imaging the actin network of various COS-7 cells. We compared images from TIRF-RIM and a commercial TIRF-SIM on a dozen similar cell samples. All TIRF-RIM images appeared well contrasted and crisp in both the dense and sparse regions of the sample [Figs. 3(a) and 3(b)]. They were free from visible artifacts except at the edges of the field of view, which were often slightly out of focus (the coverslip being not perfectly plane). On the other hand, TIRF-SIM images showed a variability in their quality. Some

cell reconstructions were almost artifact-free (Supplement 1 Fig. 9), but others displayed notable grid artifacts, introducing spurious parallel lines or honeycomb structures. These artifacts appeared at different places depending on the cells, suggesting they were due to sample-induced aberrations and light leaks [Figs. 3(c) and 3(d)].

4. PODOSOME IMAGING USING TIRF-RIM

In this section, we demonstrate the potential of TIRF-RIM for live-cell imaging. We investigated the dynamics of paxillin and F-actin filaments in podosomes formed at the basal membrane of macrophages [24].

We first checked the resolution of TIRF-RIM by imaging in live conditions the basal membrane of a fixed macrophage labeled with GFP-paxillin. TIRF-RIM reconstruction obtained from 400 speckled images was significantly better resolved (2.25 fold) than the standard TIRFM image with a resolution of 86 nm estimated by Fourier ring correlation (FRC) for TIRF-RIM, as compared to 194 nm for TIRF (Supplement 1 Fig. 10). In particular, TIRF-RIM confirmed that the paxillin formed nanoclusters within the podosomes' adhesion rings [24,25].

We then considered a live specimen labeled with GFP-paxillin and mCherry-tagged Lifeact (F-actin). We recorded a stream of

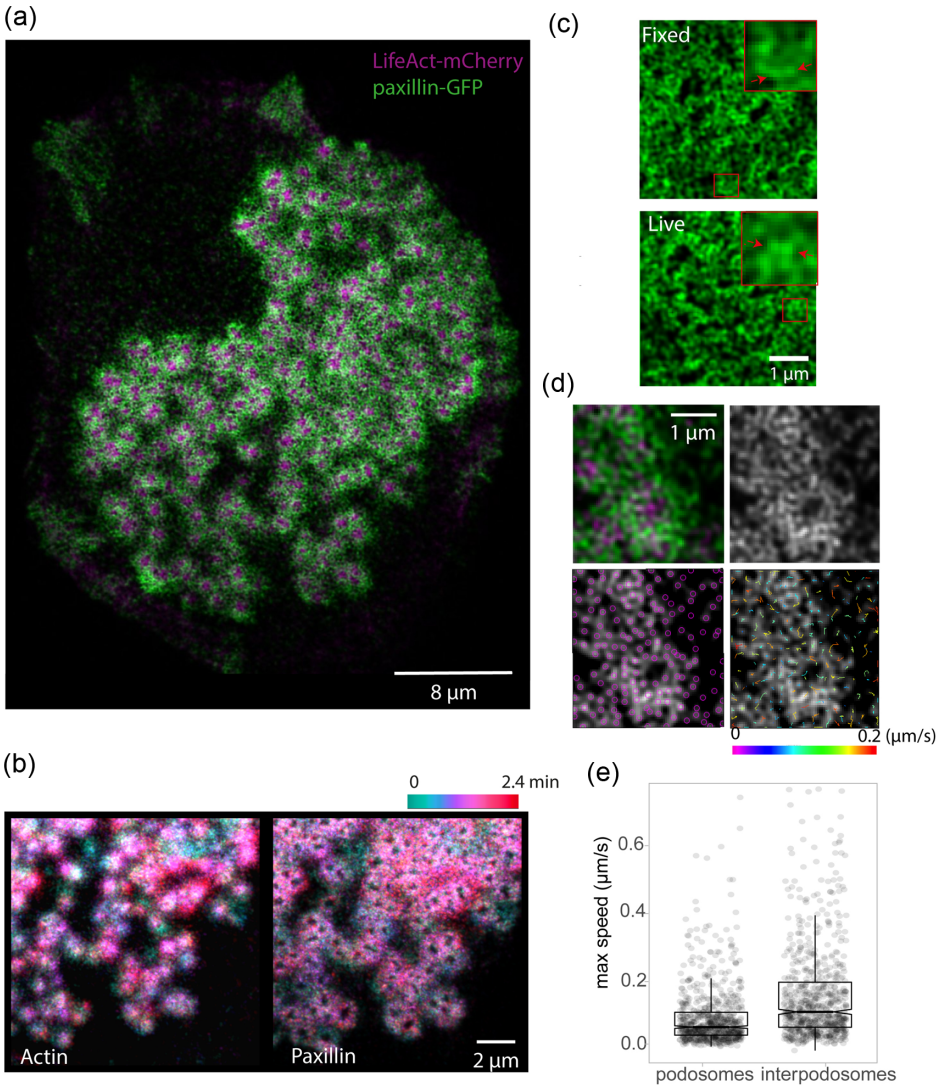

Fig. 4. Dynamic TIRF-RIM imaging of paxillin and F-actin in macrophage podosomes. The TIRF-RIM images are reconstructed from stacks of 100 speckled images recorded every 10 ms (Visualization 1 and Visualization 3) or every 1.2 ms (Visualization 2). The interleaved procedure (forming TIRF-RIM images from overlapping stacks shifted by 12 images) is applied to Visualization 3 to give an apparent temporal resolution of 0.12 s. (a) Two-color TIRF-RIM image of the F-actin network (magenta) and paxillin (green) extracted from Visualization 1. (b) Temporally color-coded image of the podosome dynamics over 3 min, obtained from Visualization 1. Most podosomes remain present, suggesting low phototoxicity. (c) Comparison between the paxillin image of a fixed macrophage (top), obtained with 400 speckled illuminations, and that of a live macrophage obtained with 100 speckled illuminations (bottom). Using Fourier ring correlation, the image resolution of the fixed sample was estimated to 86 nm, slightly better than that of the live sample, 96 nm. The insets show the ability of TIRF-RIM to distinguish nanoclusters in both the fixed and live samples. The blur induced by the paxillin dynamics and the granular noise coming from the small number of illuminations are negligible. (d) Study of the paxillin trajectories using TrackMate (Fiji software) on Visualization 3. Top left: zoom on the bicolor image of a podosome. Top right: zoom on the Paxillin image only. Bottom left, the purple circles indicate the paxillin nanoclusters detected by the tracker. Bottom right, trajectories of the nanoclusters (the color codes for the maximum speed, bounded here to 0.2 μms^{-1} for easing the representation). Tracking nanoclusters on a fixed macrophage yields a sensitivity of 20 nm/s (Supplement 1 Fig. 11 and Visualization 3). (e) Nanocluster maximum speed. Nanoclusters within 1 µm of a podosome ring center (podosomes) are slower than the others (interpodosomes).

38,000 two-color speckled images taken every 10 ms for a total observation time of 6.33 min. TIRF-RIM reconstructions were formed from stacks of 100 speckled images (1 s per super-resolved image). Figure 4(a) displays a two-color TIRF-RIM image showing the paxillin nanoclusters surrounding the F-actin podosome cores [26] extracted from Visualization 1. The spatial resolution of the live paxillin image was estimated by FRC to 96 nm, i.e., close to that obtained with the fixed sample (86 nm) (Supplement 1 Fig. 9 and Fig. 4C). The comparison between the fixed and live sample image indicates that the blur induced by the protein displacements and the granular noise due to the illumination inhomogeneity (inevitably more important with 100 speckled illuminations than with 400) are not an issue [Fig. 4(c)].

The temporally color-coded image shown in Fig. 4(b), obtained from Visualization 1, illustrates the podosome dynamics at a large temporal scale (one image every 34 s). It is seen that most podosomes remain visible during the observation time, which confirms the weak phototoxicity of TIRF-RIM (the podosomes' average lifetime on a glass surface is about 10 min [27]).

The podosome dynamics at a small temporal scale were obtained by recording a stream of 1000 speckled images taken every 1.2 ms. The super-resolved images, formed from successive stacks of 100 speckled images (temporal resolution of 0.12 s), exhibited a FRC spatial resolution estimated as 120 nm. The displacements of paxillin nanoclusters between the podosome cores could be clearly observed (Visualization 2).

In Visualization 3, we investigated the interest of the interleaved or rolling procedure for studying paxillin dynamics [28]. We considered the 38,000 speckled images of Visualization 1 and formed super-resolved images from overlapping stacks of 100 speckled images shifted by 12 images. Thus, the apparent temporal resolution of Visualization 3 was 0.12 s as in Visualization 2. The dynamics observed in Visualization 3 did not look significantly different from those of Visualization 2.

We tracked the nanoclusters during the 3.6 s of Visualization 3, and estimated the apparent maximum speed of the clusters [Figs. 1(d) and 4(e)]. Surprisingly, we observed that the paxillin nanoclusters moved more slowly when they were close to a podosome core (within 1 μm of the podosome ring center) than when they were further away (maximum speed medians about 70 nm/s in the podosomes and 120 nm/s in interpodosomes). A control experiment applying the same procedure to a fixed macrophage showed that these speed values were well above the sensitivity of the tracker, about 20 nm/s (Supplement 1 Fig. 11and Visualization 3).

5. DISCUSSION

In this work, we combined the advantages of TIRF and RIM methods to provide super-resolved fluorescence images close to the coverslip. TIRF-RIM consists in recording multiple images of the sample under different evanescent speckled illuminations and reconstructing a super-resolved image from their variance (Fig. 1). Our results show that TIRF-RIM outperforms standard TIRFM by more than two-fold improvement of the resolution and a much better contrast with minimal out-of-focus blur (Fig. 2 and Supplement 1 Fig. 6). TIRF-RIM could disclose the presence of two lines separated by 60 nm over a 30 μm × 30 μm field of view, reaching the performance of the sparse-SIM technique [14] but without introducing any *a priori* information on the sample [Fig. 2(d)]. Using standard objectives with NA = 1.49, TIRF-RIM could resolve the ring shape of clathrin-coated pits of fixed COS-7 cell (Fig. 2B) and image the basal surface of fixed macrophages at a 86 nm resolution (Supplement 1 Fig. 10).

The most remarkable advantage of TIRF-RIM is its robustness to the various imaging conditions. As it does not require knowledge of the illuminations, it is not affected by large Stokes shifts [compare Fig. 2(b) and Supplement 1 Fig. 8B] or distortion of the excitation patterns. TIRF-RIM was used to image the actin network of a dozen of fixed cell samples. All the images presented a high contrast and high resolution in the dense and sparse regions, without visible artifacts (except for some defocusing at the edges of the field of view) [Figs. 3(a) and 3(b)]. In comparison, the images provided by a commercial TIRF-SIM on similar samples were of variable quality, some of them being affected by grid artifacts appearing at seemingly random positions in the field of view [Figs. 3(c) and 3(d)].

The temporal resolution of TIRF-RIM benefited from the observation that 100 speckled images were enough to obtain satisfactory reconstructions [Fig. 4(c)]. TIRF-RIM reconstructions seemed less affected by the residual granular artifacts that appeared in standard RIM reconstructions when the number of speckled images was insufficient; see Supplement 1 Fig. 12. This is likely due to the difference in the illumination patterns, the more closely packed and smaller light grains of TIRF-like speckles covering the sample plane more homogeneously than the dispersed grains of propagative speckles [Fig. 1(b)].

TIRF-RIM two-color imaging of the dynamics of macrophages podosomes over 6 min, at a spatio-temporal resolution of 96 nm in 1 s, demonstrated the great interest of the method with its low phototoxicity for live-cell imaging during long periods of time and large fields of view (Visualization 1). For shorter observation times, TIRF-RIM could follow the trajectory of individual paxillin nanoclusters at a spatio-temporal resolution of 120 nm at in 0.12 s (Visualization 2).

The dynamics of components of integrin adhesion sites were previously investigated by super-resolution microscopy but never at this spatio-temporal resolution. As a comparison, PALM SOFI and TIRF-SIM allowed the observation of focal adhesion sites with a 100 nm resolution but only a 10 s temporal resolution [29,30]. Bayesian localization microscopy offered a high spatial resolution of 50 nm but with a temporal resolution of 4 s [31]. Last, sptPALM imaging of focal adhesion components achieved an impressive 50 nm resolution at 50 Hz [32,33], but the method focused on single protein tracking and missed the protein clustering.

Analysis by TIRF-RIM of individual paxillin nanocluster trajectories revealed that their moving speed was lower within podosome rings than outside podosomes. It will be interesting to compare the dynamics of paxillin nanoclusters with those of other adhesion-related proteins and to address the molecular mechanisms orchestrating these dynamics.

In conclusion, while TIRF-SIM remains the method of choice for imaging at very high temporal resolution (when the speed limit is set essentially by the camera framerate), TIRF-RIM appears as an attractive alternative for high throughput super-resolved imaging, thanks to its robust image quality, ease of use, and overall resolution performance.

6. METHODS

A. Principles of TIRF-RIM Reconstruction AlgoRIM

The theoretical fundations of RIM are described in [21,34]. Here, we recall the main steps of the theory and reconstruction procedure adapted to the TIRF configuration.

In TIRF-RIM, the fluorophore density of the sample is recovered from the variance of M low-resolution images (I_m, $m = 1 \dots M$) obtained under M different speckled illuminations which are formed through an annular aperture. The transverse spatial frequency cut-off of the microscope point spread function is noted $\nu_{\text{obs}} = 2\text{NA}_{\text{obs}}/\lambda_{\text{obs}}$, and that of a speckle pattern is $\nu_{\text{ill}} = 2\text{NA}_{\text{ill}}/\lambda_{\text{ill}}$, where $\lambda_{\text{obs(ill)}}$ is the wavelength of the fluorescence (illumination) and $\text{NA}_{\text{obs(ill)}}$ is the numerical aperture of the microscope objective (of the TIRF annular aperture outer radius). As in SIM, each low-resolution image, I_m, is sensitive to the sample spectrum up to $(\nu_{\text{obs}} + \nu_{\text{ill}})$. We introduce the empirical variance of the speckled images as

$$V^M = \frac{1}{M}\sum_{m=1}^{M} I_m^2 - \left(\frac{1}{M}\sum_{m=1}^{M} I_m\right)^2 \tag{1}$$

and the asymptotic variance of the speckled images as

$$V^\infty = \langle I^2\rangle - \langle I\rangle^2, \tag{2}$$

where $\langle\rangle$ stands for averaging over an infinite number of realizations of speckled illuminations (V^∞ is the limit of V^M when M tends towards infinity). The variance of the speckled images is *a priori* sensitive to the sample frequencies up to $(\nu_{\text{obs}} + \nu_{\text{ill}})$, while, because of the square of the images involved in its formation, its frequency cut-off is $2\nu_{\text{obs}}$. We have shown in [21] that, if $\nu_{\text{obs}} = \nu_{\text{ill}}$, there is a bijection between the sample and the variance spatial frequencies up to $2\nu_{\text{obs}}$, which paves the way towards a two-fold resolution gain. This demonstration points out the fundamental difference between RIM and stochastic optical fluctuation imaging [6] in which the random images are obtained with a spatially uncorrelated stochastic excitation of the fluorophores. In this case, there is no possible bijection between the variance and the sample frequencies in an extended Fourier domain (except if the fluorophore density is binary).

In RIM, we recover the sample frequencies from the variance with an inversion procedure, named algoRIM, which is described in [19,22]. The code is accessible [35]. AlgoRIM requires only knowledge of the two-dimensional observation point spread function h_{obs} and speckle autocorrelation C.

Hereafter, we recall the main steps and assumptions of AlgoRIM adapted to TIRF imaging. We assume that the useful signal recorded by the camera comes only from the thin sample slice that is located at the object focal plane coinciding with the coverslip surface. The fluorophore density of the sample is

$$\rho(\mathbf{r}', z') = \rho(\mathbf{r}')\delta(z'), \tag{3}$$

where $\mathbf{r}'$ indicates a position in the focal plane and z' is the coordinate along the optical axis with $z' = 0$ corresponding to the object focal plane.

The intensity recorded at $\mathbf{r}$ by the microscope camera, when the fluorophore density ρ is excited by the mth speckled illumination S_m, reads

$$Y_m(\mathbf{r}) = \int \rho(\mathbf{r}')S_m(\mathbf{r}')h_{\text{obs}}(\mathbf{r}-\mathbf{r}')\mathrm{d}\mathbf{r}' + b(\mathbf{r}), \tag{4}$$

which can be cast in condensed form as

$$Y_m(\mathbf{r}) = [\rho S_m \star h_{\text{obs}}](\mathbf{r}) + b(\mathbf{r}), \tag{5}$$

where $b(\mathbf{r})$ is the residual out-of-focus fluorescence that is assumed not to depend on S_m and $\star$ stands for the convolution operator.

The recorded intensity of each raw speckled image is deteriorated with uncorrelated zero-mean noise $\eta(\mathbf{r})$ (Poisson and electronic noise), so that the model of the speckled image is

$$I_m(\mathbf{r}) = Y_m(\mathbf{r}) + \eta_m(\mathbf{r}). \tag{6}$$

In a first step, we estimate the noise variance $\langle\eta^2(\mathbf{r})\rangle = w(\mathbf{r})$. We observe that the spectrum of the useful signal in I_m belongs to the disk of radius ν_{obs}, while the spectrum of the noise η covers the whole Fourier space. Thus, we estimate w from the empirical variance of a filtered version of I_m in which all the spatial frequencies below ν_{obs} have been suppressed [22].

Then, each raw speckled image is prefiltered (using a Wiener filter [36]) to remove the noise beyond the Fourier support of the observation point spread function and enhance the frequencies close to the cut-off. We introduce the Fourier transform of the point spread function as

$$\tilde{h}_{\text{obs}}(\boldsymbol{\nu}) = \int h_{\text{obs}}(\mathbf{r})e^{2i\pi\boldsymbol{\nu}\cdot\mathbf{r}}\mathrm{d}\mathbf{r}, \tag{7}$$

and the filter

$$\tilde{f}(\boldsymbol{\nu}) = \frac{\tilde{h}^*_{\text{obs}}(\boldsymbol{\nu})}{|\tilde{h}_{\text{obs}}(\boldsymbol{\nu})|^2 + \epsilon}, \tag{8}$$

where a^* stands for the complex conjugate of a, and ϵ is the (assumed to be constant) power spectral density of the noise of the speckled images and is, in practice, adjusted by eye. The prefiltered speckled images are calculated as

$$i_m(\mathbf{r}) = [I_m \star f](\mathbf{r}). \tag{9}$$

The empirical variance V^M of the prefiltered speckled images is formed with M varying between 50 and 400 in most applications. Then, V^M is compared to the asymptotic variance, whose expression is given by [19,34]

$$V^\infty(\mathbf{r}) = \iint \rho(\mathbf{r}_1)H_{\text{obs}}(\mathbf{r}-\mathbf{r}_1)C(\mathbf{r}_1-\mathbf{r}_2)\rho(\mathbf{r}_2) \times H_{\text{obs}}(\mathbf{r}-\mathbf{r}_2)d\mathbf{r}_1 d\mathbf{r}_2 + W(\mathbf{r}), \tag{10}$$

where $H_{\text{obs}}(\mathbf{r}) = h_{\text{obs}} \star f$ and $W(\mathbf{r}) = w \star f^2$ is the noise variance of the prefiltered speckled images.

The fluorophore density is reconstructed iteratively so as to minimize the distance F between the asymptotic model and the empirical variance

$$F(\rho) = |V^M(\mathbf{r}) - V^\infty[\rho](\mathbf{r})|^2, \tag{11}$$

where the dependence of V^∞ to ρ has been made explicit. The minimization is performed thanks to a standard descent algorithm. The only difficulty lays in the computation of the asymptotic variance for each new estimation of the fluorophore density as it involves a computationally expensive quadruple integral [Eq. (10)]. To ease this task and accelerate the reconstruction, we have used the property that $T(\boldsymbol{u}, \boldsymbol{v}) = H_{\text{obs}}(\boldsymbol{u})C(\boldsymbol{u}-\boldsymbol{v})H_{\text{obs}}(\boldsymbol{v})$

is a positive definite operator, which can be decomposed over a basis of singular eigenvectors (singular value decomposition),

$$T(\boldsymbol{u}, \boldsymbol{v}) = \sum_{n=1}^{\infty} \mu_n Q_n(\boldsymbol{u}) Q_n(\boldsymbol{v}), \tag{12}$$

where the eigenvalues μ_n are positive and decreasing and Q_n are orthonormal eigenfunctions. Usually, less than 10 eigenfunctions are required to calculate V^{∞} with enough accuracy.

In all the reconstructions, we used a theoretical estimation of the speckle autocorrelation C and of the observation point spread function h_{obs}. Under the scalar approximation, C can be modeled as [19]

$$C(\mathbf{r}) = \left| \int |\tilde{g}|^2(\boldsymbol{\nu}) \exp^{2i\pi \boldsymbol{\nu}\cdot\mathbf{r}} \, \mathrm{d}\boldsymbol{\nu} \right|^2, \tag{13}$$

where $\tilde{g}$ is the pupil function of the objective. For standard speckles, $\tilde{g}$ is nonzero for $\nu < \mathrm{NA}_{\text{ill}}/\lambda_{\text{ill}}$. For TIRF speckles, in presence of the annular aperture, $\tilde{g}$ is nonzero for $\mathrm{NA}_{\text{low}}/\lambda_{\text{ill}} < \nu < \mathrm{NA}_{\text{ill}}/\lambda_{\text{ill}}$, where $\mathrm{NA}_{\text{low,ill}}$ are the numerical apertures defined by the inner and outer radii of the annulus, as illustrated in Fig. 1(b). Note that Eq. (13) is also used to model the point spread function by replacing λ_{ill} by λ_{obs}. We verified that the experimental autocorrelations of the standard speckles (without the annular aperture) and of the TIRF speckles (with the annular aperture) were close to the theoretical ones in Supplement 1 Fig. 5.

B. TIRF-RIM and TIRF Experiments

All TIRF-RIM experiments were performed on the RIM inverted microscope setup detailed in [19]. We used an inverted microscope (TEi Nikon) with a TIRF objective 100× magnification (CFI SR APO 100× NA 1.49 Nikon) with an immersion oil of refractive index 1.515 similar to that of the glass coverslip. A diode laser (Oxxius) with wavelength centered at 488 nm (LBX-488-200-CSB) was used in all the experiments. The bicolor images were obtained with a single illumination (at 488 nm), and the fluorescence was recorded on two cameras with different fluorescence filters. This simple excitation scheme was made possible by the relatively large excitation spectrum of the fluorophores and by the insensitivity of TIRF-RIM to large Stokes shifts (Supplement 1 Fig. 8).

The collimated 8.8 mm TEM00 beam illuminated a fast spatial light phase binary modulator (SLM, QXGA Fourth dimension) placed at a plane conjugated with the image plane of the objective. A first afocal telescope (lenses L1 and L2 with focal length of 250 mm, L3 with focal length 135 mm) produced a secondary Fourier plane. The evanescent illumination at the glass–water interface was obtained by placing an annular aperture of central radius $R = 6.05$ mm and width 300 μm at the secondary Fourier (or backfocal) plane of the objective to block the waves propagating below the critical angle.

The fluorescence was collected on one or two sCMOS cameras (OrcaFlash fusion) after passing through the dichroic D1 (Semrock DI02-R488-25 × 36) and a Stop Line quad-Notch filter (Semrock NF03-405/488/561/635E-25) for blocking the illumination. The fluorescence light was sent towards two different cameras thanks to the dichroic D2 (Semrock Di02-R561-25 × 36). We used two relay lenses L4 and L5 (focal lengths equal to 200 mm), image lenses L6 and L7 (200 mm)m and two bandpass filters (Semrock FF01-514/30-25 for Green Fluorescence Protein and RFP 330 Smerock FF01-650/92 for mcherry). The triggering of the illumination, SLM, and camera is described in Mangeat *et al*. [19]. The synchronization of the hardware (Z-platform, cameras, microscope, laser, and SLM) is performed by an improved version of the commercial software INSCOPER.

The TIRF images were always obtained by summing the prefiltered speckled images (which ensured a similar photon budget for the comparison and the same Wiener deconvolution).

C. TIRF-SIM Experiments

All of the TIRF-SIM experiments were performed at the imaging facilities of Aix-Marseille University, INP, which is a Nikon Center of Excellence. We used a Nikon N-SIM-S microscope to image COS-7 cells stained for actin via classical two-beam TIRF-SIM [37]. Cells were mounted in a Ludin chamber in 0.1M phosphate buffer. The sample was illuminated using a 488 nm laser with two opposite beams at the periphery of the back focal plane of a 100×, 1.49 NA objective, with nine images (3 phases × 3 orientations; 16-bit, 1024 × 1024 pixels at 65 nm/pixel) captured over a 50 ms exposure time by an Hamamatsu Fusion BT sCMOS camera. The raw images were then processed using the N-SIM module of the NIS Elements software, resulting in a 32-bit, 2048 × 2048 pixel reconstructed image at 32.5 nm/pixel.

D. Sample Preparation

Cells were briefly extracted in Triton X-100/glutaraldehyde and then fixed using glutaraldehyde, before being quenched, blocked, and stained with anticlathrin heavy chain primary antibodies (polyclonal rabbit ab21679, abcam) revealed with donkey antirabbit secondary antibodies conjugated to Alexa Fluor 488 or Alexa Fluor 555, and antialpha tubulin primary antibodies (monoclonal mouse clones B-5-1-2 and DM1a, Sigma) revealed with donkey antimouse secondary antibodies conjugated to Alexa Fluor 555. To stain actin, cells were incubated with phalloidin-Atto488 at the end of the staining procedure.

For live imaging, macrophages were transduced with mCherry-tagged Lifeact and GFP-paxillin lentiviruses (BiVic facility, Toulouse, France) for three days as previously described [19]. Macrophages were placed on a FluoroDish (WPI FD35-100) with cells facing down and immersed with RPMI without phenol red, supplemented with 10% FCS (Thermo Fisher 32404-014). During the imaging experiments, the cell samples were maintained at 37°C in humidified 5% CO2 atmosphere.

Funding. Agence Nationale de la Recherche (3D-RIM-2020/2024).

Disclosures. The authors declare no conflicts of interest.

Data availability. Data are available upon reasonable request.

Supplemental document. See Supplement 1 for supporting content.

REFERENCES

1. D. Axelrod, "Cell-substrate contacts illuminated by total internal reflection fluorescence," J. Cell Biol. **89**, 141–145 (1981).
2. R. Fiolka, "Clearer view for TIRF and oblique illumination microscopy," Opt. Express **24**, 29556–29567 (2016).
3. E. J. Ambrose, "A surface contact microscope for the study of cell movements," Nature **178**, 1194 (1956).
4. M. Brunstein, K. Hérault, and M. Oheim, "Eliminating unwanted far-field excitation in objective-type tirf. Part II. Combined evanescent-wave

excitation and supercritical-angle fluorescence detection improves optical sectioning," Biophys. J. **106**, 1044–1056 (2014).
5. T. J. Gould, J. R. Myers, and J. Bewersdorf, "Total internal reflection STED microscopy," Opt. Express **19**, 13351–13357 (2011).
6. T. Dertinger, R. Colyera, G. Iyer, S. Weiss, and J. Enderlein, "Fast, background-free, 3d super-resolution optical fluctuation imaging (SOFI)," Proc. Natl. Acad. Sci. USA **106**, 22287–22292 (2009).
7. J. Cnossen, T. Hinsdale, R. Ø. Thorsen, M. Siemons, F. Schueder, R. Jungmann, C. S. Smith, B. Rieger, and S. Stallinga, "Localization microscopy at doubled precision with patterned illumination," Nat. Methods **17**, 59–63 (2020).
8. L. Schermelleh, A. Ferrand, T. Huser, C. Eggeling, M. Sauer, O. Biehlmaier, and G. P. Drummen, "Super-resolution microscopy demystified," Nat. Cell Biol. **21**, 72–84 (2019).
9. G. Jacquemet, A. F. Carisey, H. Hamidi, R. Henriques, and C. Leterrier, "The cell biologist's guide to super-resolution microscopy," J. Cell Sci. **133**, jcs240713 (2020).
10. E. Chung, D. Kim, Y. Cui, Y.-H. Kim, and P. T. So, "Two-dimensional standing wave total internal reflection fluorescence microscopy: Superresolution imaging of single molecular and biological specimens," Biophys. J. **93**, 1747–1757 (2007).
11. R. Fiolka, M. Beck, and A. Stemmer, "Structured illumination in total internal reflection fluorescence microscopy using a spatial light modulator," Opt. Lett. **33**, 1629–1631 (2008).
12. D. Li, L. Shao, B. C. Chen, X. Zhang, M. Zhang, B. Moses, D. E. Milkie, J. R. Beach, J. A. Hammer, M. Pasham, T. Kirchhausen, M. A. Baird, M. W. Davidson, P. Xu, and E. Betzig, "Extended-resolution structured illumination imaging of endocytic and cytoskeletal dynamics," Science **349**, aab3500 (2015).
13. X. Huang, J. Fan, L. Li, H. Liu, R. Wu, Y. Wu, L. Wei, H. Mao, A. Lal, P. Xi, L. Tang, Y. Zhang, Y. Liu, S. Tan, and L. Chen, "Fast, long-term, super-resolution imaging with hessian structured illumination microscopy," Nat. Biotechnol. **36**, 451–459 (2018).
14. W. Zhao, S. Zhao, L. Li, *et al.*, "Sparse deconvolution improves the resolution of live-cell super-resolution fluorescence microscopy," Nat. Biotechnol. **40**, 606–617 (2022).
15. M. Guo, P. Chandris, J. P. Giannini, A. J. Trexler, R. Fischer, J. Chen, H. D. Vishwasrao, I. Rey-Suarez, Y. Wu, X. Wu, C. M. Waterman, G. H. Patterson, A. Upadhyaya, J. W. Taraska, and H. Shroff, "Single-shot super-resolution total internal reflection fluorescence microscopy," Nat. Methods **15**, 425–428 (2018).
16. J. Demmerle, C. Innocent, A. J. North, G. Ball, M. Müller, E. Miron, A. Matsuda, I. M. Dobbie, Y. Markaki, and L. Schermelleh, "Strategic and practical guidelines for successful structured illumination microscopy," Nat. Protoc. **12**, 988–1010 (2017).
17. K. Wicker, O. Mandula, G. Best, R. Fiolka, R. Heintzmann, E. Betzig, G. H. Patterson, R. Sougrat, W. Lindwasser, S. Olenych, J. S. Bonifacino, M. W. Davidson, J. Lippincott-Schwartz, and H. F. Hess, "Phase optimisation for structured illumination microscopy," Opt. Express **21**, 2032–2049 (2013).
18. J. Roth, J. Mehl, and A. Rohrbach, "Fast TIRF-SIM imaging of dynamic, low-fluorescent biological samples," Biomed. Opt. Express **11**, 4008–4026 (2020).
19. T. Mangeat, S. Labouesse, M. Allain, *et al.*, "Super-resolved live-cell imaging using random illumination microscopy," Cell Rep. Methods **1**, 100009 (2021).
20. S. Labouesse, J. Idier, A. Sentenac, and T. Mangeat, "Image variance based random illumination microscopy," hal-02495824 (2020).
21. S. Labouesse, J. Idier, A. Sentenac, M. Allain, and T. Mangeat, "Proof of the resolution-doubling of random illumination microscopy using the variance of the speckled images," in *29th European Signal Processing Conference (EUSIPCO)* (IEEE, 2021), pp. 1159–1162.
22. S. Labouesse, J. Idier, A. Sentenac, T. Mangeat, and M. Allain, "Random illumination microscopy from variance images," in *28th European Signal Processing Conference (EUSIPCO)* (IEEE, 2021), pp. 785–789.
23. A. Negash, S. Labouesse, N. Sandeau, M. Allain, H. Giovannini, J. Idier, R. Heintzmann, P. C. Chaumet, K. Belkebir, and A. Sentenac, "Improving the axial and lateral resolution of three-dimensional fluorescence microscopy using random speckle illuminations," J. Opt. Soc. Am. A **33**, 1089–1094 (2016).
24. S. Linder and P. Kopp, "Podosomes at a glance," J. Cell Sci. **118**, 2079–2082 (2005).
25. K. van den Dries Koen, L. Stefan, M.-P. Isabelle, and P. Renaud, "Probing the mechanical landscape—new insights into podosome architecture and mechanics," J. Cell Sci. **132**, jcs236828 (2019).
26. M. B. M. Meddens, E. Pandzic, J. A. Slotman, D. Guillet, B. Joosten, S. Mennens, L. M. Paardekooper, A. B. Houtsmuller, K. van den Dries, P. W. Wiseman, and A. Cambi, "Actomyosin-dependent dynamic spatial patterns of cytoskeletal components drive mesoscale podosome organization," Nat. Commun. **7**, 13127 (2016).
27. A. Labernadie, A. Bouissou, P. Delobelle, S. Balor, R. Voituriez, A. Proag, I. Fourquaux, C. Thibault, C. Vieu, R. Poincloux, G. M. Charrière, and I. Maridonneau-Parini, "Protrusion force microscopy reveals oscillatory force generation and mechanosensing activity of human macrophage podosomes," Nat. Commun. **5**, 5343 (2014).
28. A. Boualam and C. J. Rowlands, "Method for assessing the spatiotemporal resolution of structured illumination microscopy (SIM)," Biomed. Opt. Express **12**, 790–801 (2021).
29. H. Deschout, T. Lukes, A. Sharipov, D. Szlag, L. Feletti, W. Vandenberg, P. Dedecker, J. Hofkens, M. Leutenegger, T. Lasser, and A. Radenovic, "Complementarity of palm and sofi for super-resolution live-cell imaging of focal adhesions," Nat. Commun. **7**, 13693 (2016).
30. S. Hu, Y. H. Tee, A. Kabla, R. Zaidel-Bar, A. Bershadsky, and P. Hersen, "Structured illumination microscopy reveals focal adhesions are composed of linear subunits," Cytoskeleton **72**, 235–245 (2015).
31. S. Cox, E. Rosten, J. Monypenny, T. Jovanovic-Talisman, D. T. Burnette, J. Lippincott-Schwartz, G. E. Jones, and R. Heintzmann, "Bayesian localization microscopy reveals nanoscale podosome dynamics," Nat. Methods **9**, 195–200 (2012).
32. T. Orré, A. Joly, Z. Karatas, B. Kastberger, C. Cabriel, R. T. Böttcher, S. Lévêque-Fort, J.-B. Sibarita, R. Fässler, B. Wehrle-Haller, O. Rossier, and G. Giannone, "Molecular motion and tridimensional nanoscale localization of kindlin control integrin activation in focal adhesions," Nat. Commun. **12**, 3104 (2021).
33. O. Rossier, V. Octeau, J. B. Sibarita, C. Leduc, B. Tessier, D. Nair, V. Gatterdam, O. Destaing, C. Albigès-Rizo, R. Tampé, L. Cognet, D. Choquet, B. Lounis, and G. Giannone, "Integrins β1 and β3 exhibit distinct dynamic nanoscale organizations inside focal adhesions," Nat. Cell Biol. **14**, 1057–1067 (2012).
34. J. Idier, S. Labouesse, M. Allain, P. Liu, S. Bourguignon, and A. Sentenac, "On the superresolution capacity of imagers using unknown speckle illuminations," IEEE Trans. Comput. Imaging **4**, 87–98 (2018).
35. http://cell-rep-meth.rim-microscope.fr.
36. M. Bertero, P. Boccacci, and C. De Mol, *Introduction to Inverse Problems in Imaging* (CRC Press, 2021).
37. P. Kner, B. B. Chhun, E. R. Griffis, L. Winoto, and M. G. Gustafsson, "Super-resolution video microscopy of live cells by structured illumination," Nat. Methods **6**, 339–342 (2009).